

Observation of non-Hermitian degeneracies in a chaotic exciton-polariton billiard

T. Gao¹, E. Estrecho¹, K. Y. Bliokh^{1,2}, T. C. H. Liew³, M. D. Fraser², S. Brodbeck⁴, M. Kamp⁴, C. Schneider⁴, S. Höfling^{4,5}, Y. Yamamoto^{6,7}, F. Nori^{2,8}, Y. S. Kivshar¹, A. G. Truscott¹, R. G. Dall¹ & E. A. Ostrovskaya¹

Exciton-polaritons are hybrid light-matter quasiparticles formed by strongly interacting photons and excitons (electron-hole pairs) in semiconductor microcavities¹⁻³. They have emerged as a robust solid-state platform for next-generation optoelectronic applications as well as for fundamental studies of quantum many-body physics. Importantly, exciton-polaritons are a profoundly open (that is, non-Hermitian^{4,5}) quantum system, which requires constant pumping of energy and continuously decays, releasing coherent radiation⁶. Thus, the exciton-polaritons always exist in a balanced potential landscape of gain and loss. However, the inherent non-Hermitian nature of this potential has so far been largely ignored in exciton-polariton physics. Here we demonstrate that non-Hermiticity dramatically modifies the structure of modes and spectral degeneracies in exciton-polariton systems, and, therefore, will affect their quantum transport, localization and dynamical properties⁷⁻⁹. Using a spatially structured optical pump¹⁰⁻¹², we create a chaotic exciton-polariton billiard—a two-dimensional area enclosed by a curved potential barrier. Eigenmodes of this billiard exhibit multiple non-Hermitian spectral degeneracies, known as exceptional points^{13,14}. Such points can cause remarkable wave phenomena, such as unidirectional transport¹⁵, anomalous lasing/absorption^{16,17} and chiral modes¹⁸. By varying parameters of the billiard, we observe crossing and anti-crossing of energy levels and reveal the non-trivial topological modal structure exclusive to non-Hermitian systems^{9,13-22}. We also observe mode switching and a topological Berry phase for a parameter loop encircling the exceptional point^{23,24}. Our findings pave the way to studies of non-Hermitian quantum dynamics of exciton-polaritons, which may uncover novel operating principles for polariton-based devices.

Studies of open quantum systems go back to Gamow's theory of nuclear α -decay developed in the early days of quantum mechanics⁴. Indeed, metastable states of a single quantum particle in a spherically symmetric potential well with semi-transparent barriers decay in time, and therefore are characterized by complex energies. Furthermore, introducing a 2D potential well with non-trivial geometry, that is, a quantum billiard, results in strongly correlated energy levels and transition to quantum chaos^{7,19,21,25-28}. Spectral degeneracies crucially determine transport and dynamical properties in both non-Hermitian and chaotic wave systems^{7-9,15-17}. In chaotic and disordered wave systems, spectral degeneracies underpin statistical properties and quantum phase transitions from localized to delocalized dynamics^{8,9}. In non-Hermitian (including PT-symmetric) systems, non-trivial topology of eigenmodes and unusual transport properties in the vicinity of exceptional points^{15-17,19} are currently under investigation. Basic non-Hermitian or stochastic dynamics have so far been studied in the context of microwave^{9,18-20,24}, optical^{15-17,19,21}, atomic^{22,26,27} and electron^{25,28} waves. However, the concepts of non-Hermiticity and quantum chaos remain largely separated from each other, owing to the lack of a simple

quantum system in which both features would be readily accessible. Moreover, it is challenging to produce artificial complex potentials with gain and loss for classical waves, as well as to observe nanoscopic electron states in solids.

Microcavity exciton-polaritons represent a unique quantum macroscopic system, which combines the main advantages of light and matter waves¹⁻³. Being bosons, exciton-polaritons can display collective quantum behaviour, Bose-Einstein condensation (BEC), when they occupy a single-particle quantum state in massive numbers. Exciton-polaritons have provided a very accessible system for studies of collective quantum behaviour because they condense at temperatures ranging from 10 K to room temperature (compared to nanokelvins for neutral atoms) and do not require painstaking isolation from the environment.

The schematics of exciton-polariton condensation under continuous-wave incoherent optical excitation conditions¹ are shown in Fig. 1a. The optical pump, far detuned from the exciton resonance in the cavity, effectively creates an incoherent reservoir of 'hot', exciton-like polaritons. Above a threshold density of the reservoir, relaxation and stimulated scattering into the coherent BEC state of exciton-polaritons dominate the dynamics. The continuously pumped condensate decays and releases coherent photons, which escape the cavity carrying all information about the condensed state. The interactions between the reservoir and condensed exciton-polaritons are responsible for the formation of effective pump-induced potentials¹⁰⁻¹². Thus, the macroscopic matter wavefunction is shaped by an optical pump and spatially resolved via free-space optical microscopy. This enables us to clearly observe and control non-Hermitian and irregular quantum dynamics.

We use a structured optical pump¹⁰⁻¹² to create a non-Hermitian potential in the shape of a Sinai billiard⁷ with a circular defect of radius R (see Fig. 1b) for condensed exciton-polaritons (see Methods for details). In our experiment, the billiard has 'soft' (inelastic) walls of a finite width and height. The main properties of eigenstates of the exciton-polariton condensate in the billiard can be described by a linear Schrödinger equation with a complex two-dimensional potential $V(\mathbf{r}) = V'(\mathbf{r}) + iV''(\mathbf{r})$. Here the real part of the potential, $V'(\mathbf{r}) \propto P(\mathbf{r})$, is the potential barrier shaped as a Sinai billiard boundary with a Gaussian envelope. The optical pump rate, $P(\mathbf{r})$, is induced by the strong repulsive interaction between the excitonic reservoir populated by the pump and the polariton BEC¹⁰⁻¹². The imaginary part of the potential, $V''(\mathbf{r}) \propto P(\mathbf{r}) - \gamma$, combines the gain profile produced by the same optical pump $P(\mathbf{r})$ with the spatially uniform loss γ due to polariton decay (Fig. 1b). Despite the strong polariton-polariton interactions, the corresponding nonlinearity mostly affects the relative population of the energy eigenstates, as well as the overall blueshift (see Methods).

Changing the radius of the defect, R , varies the geometry of the billiard and hence affects the energy levels. Figures 1c and d show the

¹Research School of Physics and Engineering, The Australian National University, Canberra, Australian Capital Territory 2601, Australia. ²Center for Emergent Matter Science, RIKEN, Wako-shi, Saitama 351-0198, Japan. ³School of Physical and Mathematical Sciences, Nanyang Technological University, Singapore 637371, Singapore. ⁴Technische Physik and Wilhelm-Conrad-Röntgen Research Center for Complex Material Systems, Universität Würzburg, Am Hubland, D-97074 Würzburg, Germany. ⁵SUPA, School of Physics and Astronomy, University of St Andrews, St Andrews KY16 9SS, UK. ⁶ImPACT Project, Japan Science and Technology Agency, Chiyoda-ku, Tokyo 102-0076, Japan. ⁷Edward L. Ginzton Laboratory, Stanford University, Stanford, California 94305-4085, USA. ⁸Physics Department, University of Michigan, Ann Arbor, Michigan 48109-1040, USA.

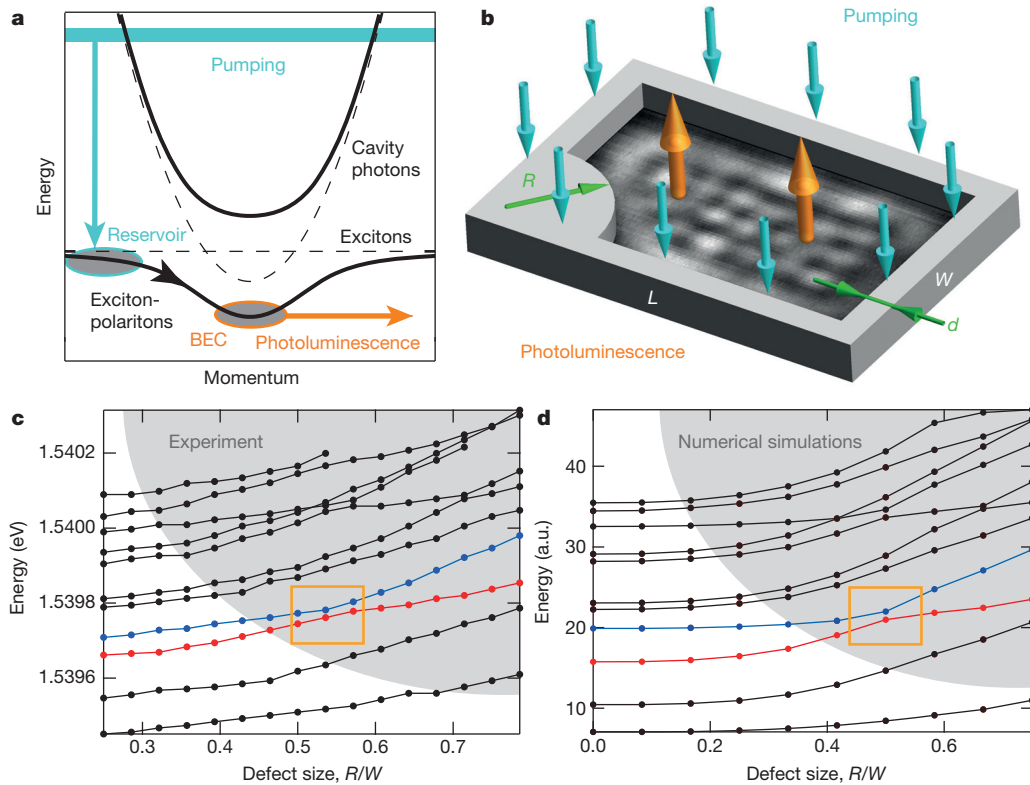


Figure 1 | Non-Hermitian exciton-polariton Sinai billiard and its spectrum. **a**, Exciton-polariton dispersion showing the upper and lower branches (solid lines) formed owing to hybridization of the cavity photon and exciton modes (dashed lines). The incoherent excitonic reservoir is continuously replenished by the optical pump (represented by the cyan arrow) and ‘feeds’ the polariton BEC (black arrow). The polariton BEC decays into cavity photoluminescence (orange arrow)^{1–3}. **b**, Schematics of the exciton-polariton Sinai billiard formed in the plane of a quantum well embedded into the microcavity (see Methods). The barrier is induced by the optical pump via the excitonic reservoir, and the square modulus of the wavefunction of the confined polariton BEC (shown in

greyscale inside the billiard) is imaged via the photoluminescence. The billiard dimensions are fixed as $W = 14 \mu\text{m}$, $L = 23 \mu\text{m}$, the radius of the defect R is varied from 0 to W , and the thickness of the walls d is varied from $3 \mu\text{m}$ to $7 \mu\text{m}$ (see Methods). **c**, **d**, Experimentally measured (**c**) and numerically simulated (**d**) spectra $E(R/W)$ for the first 11 modes of the billiard in arbitrary units (a.u.). With growing R , numerous degeneracies and quasi-degeneracies proliferate in the grey area, which is a signature of the transition to quantum chaos in the Hermitian Sinai billiard⁷. Topological properties of two near-degenerate modes (red and blue in the orange rectangles) are analysed in detail in Figs 2–4.

experimentally measured and numerically computed energy spectra $E(R)$ of the first 11 levels as a function of R . Variations of the shape of the 2D potential tune eigenvalues of different modes at different rates, and as a result some energy levels approach each other at certain values of R . It can be seen (Fig. 1c, d) that multiple degeneracies (or near-degeneracies) appear in the spectrum. In a ‘hard-wall’ Hermitian Sinai billiard, the proliferation of degeneracies is a signature of the transition from regular to chaotic dynamics⁷. Although our exciton-polariton billiard has ‘soft’ walls and can generically exhibit mixed regular-chaotic behaviour²⁷, we clearly observe multiple degeneracies similar to the ‘hard-wall’ case⁷. In Hermitian billiards, the levels generically avoid crossing (that is, they anti-cross) in the vicinity of degeneracies, which correspond to the average level repulsion and Wigner distribution of the nearest-neighbour energy spacings⁸. In contrast, the non-Hermitian systems can exhibit both crossings and anti-crossings of levels^{9,19–22}. This is because the energy eigenvalues in non-Hermitian systems are complex: the real part and imaginary parts correspond to the real energies and linewidths of the modes, respectively. A crossing of the energies is accompanied by an anti-crossing of the linewidths and vice versa. In our experiment, we measure the spectral profile of the cavity photoluminescence at a particular spatial position and extract both peak energies and widths of spectral resonances (see Methods). Crossings as well as anti-crossings of real energy levels are clearly seen both in experiments (Fig. 1c) and numerical simulations (Fig. 1d).

To observe the transition between crossing and anti-crossing for the same near-degenerate pair of eigenvalues, a second control parameter

needs to be varied. In our exciton-polariton billiard, this additional parameter is the thickness, d , of the billiard walls. Provided the internal area of the billiard remains unchanged, this parameter does not affect the geometry of the billiard and primarily controls the imaginary part V'' of the non-Hermitian potential barrier. Figure 2 shows one pair of billiard modes highlighted in Fig. 1c in the vicinity of a near-degeneracy for two values of the control parameter d . One can clearly see the anti-crossing (crossing) behaviour of the real (imaginary) parts of the complex eigenenergies in the billiard with thick walls (Fig. 2a, c) and the opposite behaviour for the thin-wall billiard (Fig. 2b, d).

Importantly, the energy-resolved real-space imaging of the photoluminescence provides all the information about complex eigenvalues as well as the spatial structure of the eigenmodes (wavefunctions). In particular, the levels shown in Fig. 2 correspond (at $R = 0$) to the third mode with three horizontal lobes and the fourth mode with two vertical lobes. The experimentally imaged and calculated spatial profiles of these eigenmodes are shown as insets in Fig. 2a, b along the eigenenergy curves. We observe that the two modes are hybridized and therefore change their spatial profiles in the near-degeneracy region, and ‘exchange’ their spatial profiles after passing it.

The behaviour of two billiard modes in the vicinity of a degeneracy can be described by a simple model of a two-level system with an effective coupling (see Methods). The corresponding non-Hermitian Hamiltonian reads^{9,18–22}:

$$\hat{H} = \begin{pmatrix} \tilde{E}_1 & q \\ q^* & \tilde{E}_2 \end{pmatrix}, \quad \tilde{E}_{1,2} = E_{1,2} - i\Gamma_{1,2} \quad (1)$$

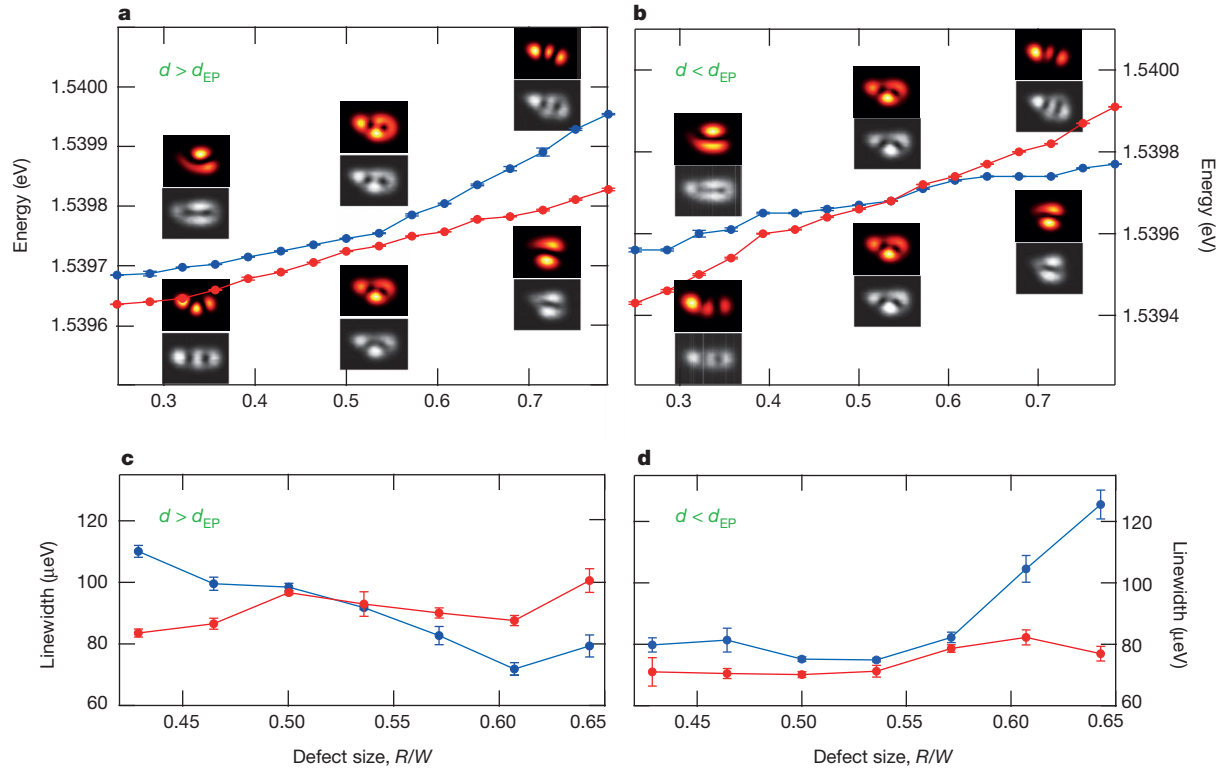


Figure 2 | Crossing and anti-crossing for two near-degenerate modes. These modes are boxed in Fig. 1c, d. **a–d**, Experimentally observed anti-crossing (**a**) and crossing (**b**) of eigenenergies of two modes in the spectrum of the exciton-polariton Sinai billiard with varying parameter R (see Fig. 1) for thick, $d \approx 6 \mu\text{m}$ (**a**, **c**), and thin, $d \approx 4 \mu\text{m}$ (**b**, **d**), billiard walls; d_{EP} is the value corresponding to the exceptional point. Panels **c** and **d** show the

Here $\tilde{E}_{1,2}$ are the complex eigenvalues of two uncoupled modes (with $E_{1,2}$ being the real energies and $\Gamma_{1,2}$ being the decay/gain rates), whereas q characterizes the coupling between these two modes (the star stands for complex conjugation). We will also use the mean complex energy $\tilde{E} = (\tilde{E}_1 + \tilde{E}_2)/2 \equiv E - i\Gamma$, and the complex energy difference $\delta\tilde{E} = (\tilde{E}_2 - \tilde{E}_1)/2 \equiv \delta E - i\delta\Gamma$. The eigenvalues of the Hamiltonian (equation (1)) are $\lambda_{1,2} = \tilde{E} \pm \sqrt{\delta\tilde{E}^2 + |q|^2}$; their real and

imaginary parts, which depend on the parameters $\delta\tilde{E} = (\delta E, \delta\Gamma)$, are shown in Fig. 3. These complex eigenvalues coalesce, $\lambda_1 = \lambda_2$, at the exceptional points (EPs)^{13–22}, where $i\delta\tilde{E}_{EP} = \pm|q|$. At these points, the eigenstates also coalesce and form a single chiral mode^{13,14,18}. Assuming that the coupling constant q is fixed, the exceptional points appear in the parameter plane as $(\delta E_{EP}, \delta\Gamma_{EP}) = (0, \pm|q|)$. We assume $\delta\Gamma > 0$ in our range of parameters, so that there is only one exceptional point in the domain of interest. The exceptional point

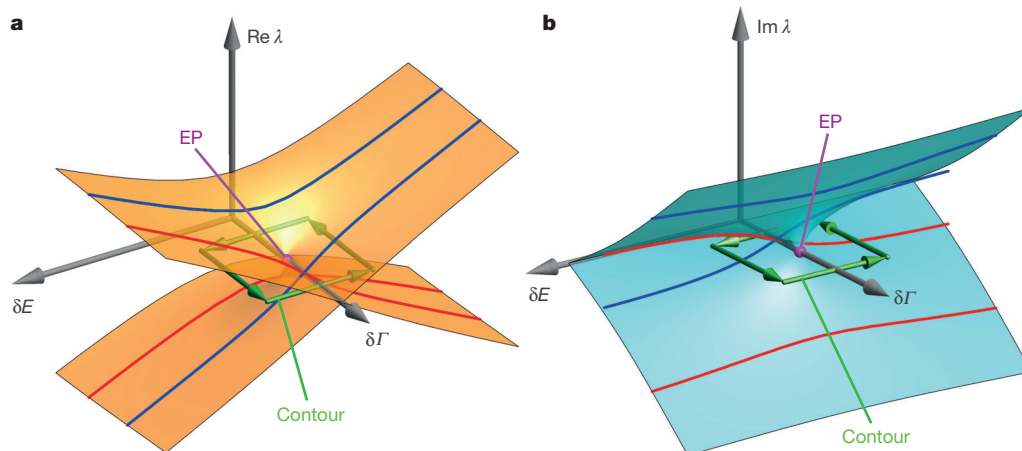


Figure 3 | Eigenvalues of a two-level non-Hermitian model in the vicinity of the exceptional point. **a**, **b**, Real (**a**) and imaginary (**b**) parts of the eigenvalues $\lambda_{1,2}$ of the model (equation (1)) as functions of two parameters, δE and $\delta\Gamma$. The exceptional point (EP) is shown in magenta. The crossing and anti-crossing of the real and imaginary parts of the eigenvalues as functions

of δE , for $\delta\Gamma < \delta\Gamma_{EP}$ and $\delta\Gamma > \delta\Gamma_{EP}$, are shown in red and blue. This is in correspondence with the experimentally observed behaviour in Fig. 2. Traversing along the green contour encircling the exceptional point in the $(\delta E, \delta\Gamma)$ plane reveals the non-trivial topology of eigenmodes, as shown in Fig. 4.

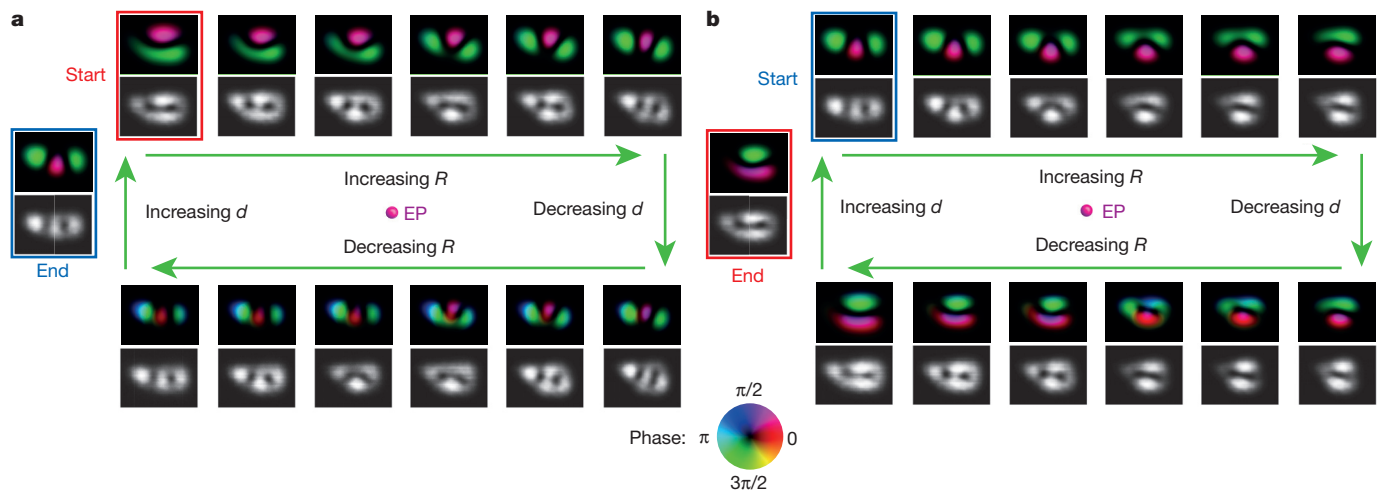


Figure 4 | Observation of the topological Berry phase acquired after circling around the exceptional point in the parameter plane. Transmutations of spatial distributions (black-and-white panels) of the selected eigenmode (from the pair shown in Fig. 2) along the closed contour in the parameter space $(R, d) \sim (\delta E, \delta I)$ encircling the exceptional point (see Fig. 3). Parameters are not varied in time during the measurements, and each distribution corresponds to the stationary mode at the corresponding parameter values.

a, b, The first loop (a) shows the transition to a different branch (mode) through the hybridization region (see explanations in text); the second loop (b) returns the mode to the original one with a π topological phase shift^{23,24}. The phases (colour panels) are inferred from comparison with the numerically calculated modes. The modes corresponding to the ‘start’ and ‘end’ points of the loop on the red (blue) branch in Figs 2a, b and 3a are boxed in red (blue).

can be encircled in the $(\delta E, \delta I)$ plane by varying these two parameters, as seen in Fig. 3.

Two parameters of the model, $(\delta E, \delta I)$, approximately correspond to the varying parameters (R, d) of our exciton-polariton billiard. The radius R mostly affects the real part of the potential, $V'(r)$, and hence the energy difference between the modes. Increasing R corresponds to a tighter spatial confinement and therefore to increasing δE . In turn, the thickness d of the billiard walls controls the gain/loss profile $V''(r)$. Different modes have different spatial overlaps with the imaginary potential $V''(r)$, and, therefore, are characterized by different integral (spatially averaged) dissipation parameters $\Gamma_{1,2}$ (see Methods). In our case, increasing d corresponds to decreasing δI . The effective coupling q in our model (equation (1)) is determined by the spatial overlap between the two modes away from the hybridization region⁹. The red and blue curves in Fig. 3 show the crossing/anti-crossing behaviour of the real and imaginary parts of the eigenvalues versus the energy difference δE for two values of the dissipation parameter: $\delta I < \delta I_{EP}$ and $\delta I > \delta I_{EP}$. This behaviour is perfectly consistent with that in the experimental Fig. 2, which means that our range of varying parameters includes the exceptional point.

The structure of the complex eigenvalues in the vicinity of the exceptional point reveals non-trivial topology of a branch-point type^{13–22}, shown in Fig. 3. Therefore, continuous encircling of the non-Hermitian degeneracy in the two-parameter plane (for example, along the green contour in Fig. 3) results in the transition to the other branch. When the contour is traversed twice, we return to the original mode, most significantly with a topological phase shift of π . This phase shift is the manifestation of the Berry phase resulting from encircling of a non-Hermitian degeneracy in a two-dimensional parameter space^{23,24}. We use the method suggested in the microwave experiment²⁴ to trace the above topological structure of two modes in the vicinity of the exceptional point. We compare the eigenmodes at neighbouring values of parameters $(\delta E, \delta I) \sim (R, d)$ along the contour encircling the exceptional point (see Fig. 3). Notably, we do not consider adiabatic evolution of modes due to variations of the parameters (R, d) in time; such evolution would be accompanied by unavoidable non-adiabatic transitions in the non-Hermitian case^{29,30}. Rather, we examine the natural topological structure and geometrical connection of stationary modes depending on the parameter values.

Figure 4 depicts the experimentally measured intensities and the corresponding numerically simulated phase profiles of the two modes from Fig. 2 for the parameter values lying on the contour encircling the exceptional point (Fig. 3). In Fig. 4a, we start on the upper branch (blue in Figs 2a and 3a) at $R < R_{EP}$, $d > d_{EP}$ and trace the eigenmode transmutation as the radius is increased to $R > R_{EP}$. This takes us from the vertical two-lobe mode, through the anti-crossing, to the horizontal three-lobe mode (still on the blue upper branch). Then, we decrease the thickness to $d < d_{EP}$ and stay on the same horizontal three-lobe mode, which now corresponds to the red branch in Figs 2b and 3a. Next, reducing the radius R takes this mode through the crossing and recovers its three-lobe structure. Increasing d closes the loop. Thus, the continuous transformation brought us from the vertical two-lobe mode (‘start’ in Fig. 4a) to the horizontal three-lobe mode (‘end’ in Fig. 4a) at the same values of the parameters. Repeating this traverse one more time (Fig. 4b) returns us to the original vertical two-lobe mode, but now with the π topological phase shift (clearly seen in the simulated phase profiles). The experimental density distribution of the modes is in very good agreement with that calculated numerically. Therefore we can associate the phase structure of the simulated spatial modes with the experimental mode profiles²⁴.

Thus, we have demonstrated the creation of highly controllable complex (non-Hermitian) potentials for exciton-polaritons, and implemented a chaotic non-Hermitian exciton-polariton billiard with multiple spectral degeneracies. We have provided detailed experimental observations of the non-trivial behaviour of complex eigenvalues and eigenmodes in the vicinity of an exceptional point. These include crossing/anti-crossing transitions as well as mode switching and topological Berry phase when encircling the exceptional point in the two-parameter plane. Our results show that the inherent non-Hermitian nature of exciton-polaritons determines their basic properties, which are crucial for transport and quantum information processing. Therefore, these features should be taken into account in future studies and applications involving confinement and manipulation of exciton-polaritons. Most importantly, this complex quantum dynamics can bring novel functionality to polariton-based devices operating at the interface between photonics and electronics. Generally, exciton-polaritons offer a novel macroscopic quantum platform for studies of non-Hermitian physics and quantum chaos at the confluence of light and matter.

Online Content Methods, along with any additional Extended Data display items and Source Data, are available in the online version of the paper; references unique to these sections appear only in the online paper.

Received 4 April; accepted 18 August 2015.

Published online 12 October 2015.

- Kasprzak, J. *et al.* Bose–Einstein condensation of exciton polaritons. *Nature* **443**, 409–414 (2006).
- Deng, H., Haug, H. & Yamamoto, Y. Exciton-polariton Bose–Einstein condensation. *Rev. Mod. Phys.* **82**, 1489–1537 (2010).
- Carusotto, I. & Ciuti, C. Quantum fluids of light. *Rev. Mod. Phys.* **85**, 299–366 (2013).
- Moiseyev, N. *Non-Hermitian Quantum Mechanics* (Cambridge Univ. Press, 2011).
- Bender, C. M. Making sense of non-Hermitian Hamiltonians. *Rep. Prog. Phys.* **70**, 947–1018 (2007).
- Savidis, P. G. *et al.* Off-branch polaritons and multiple scattering in semiconductor microcavities. *Phys. Rev. B* **64**, 075311 (2001).
- Berry, M. V. Quantizing a classically ergodic system: Sinai's billiard and the KKR method. *Ann. Phys.* **131**, 163–216 (1981).
- Guhr, T., Müller-Groeling, A. & Weidenmüller, H. A. Random-matrix theories in quantum physics: common concepts. *Phys. Rep.* **299**, 189–425 (1998).
- Bliokh, K. Y., Bliokh, Y. P., Freilikher, V., Genack, A. Z. & Sebbah, P. Coupling and level repulsion in the localized regime: from isolated to quasiextended modes. *Phys. Rev. Lett.* **101**, 133901 (2008).
- Tosi, G. *et al.* Sculpting oscillators with light within a nonlinear quantum fluid. *Nature Phys.* **8**, 190–194 (2012).
- Sanvitto, D. *et al.* All-optical control of the quantum flow of a polariton condensate. *Nature Photon.* **5**, 610–614 (2011).
- Dall, R. *et al.* Creation of orbital angular momentum states with chiral polaritonic lenses. *Phys. Rev. Lett.* **113**, 200404 (2014).
- Berry, M. V. Physics of non-Hermitian degeneracies. *Czech. J. Phys.* **54**, 1039–1047 (2004).
- Heiss, W. D. The physics of exceptional points. *J. Phys. Math. Gen.* **45**, 444016 (2012).
- Guo, A. *et al.* Observation of PT-symmetry breaking in complex optical potentials. *Phys. Rev. Lett.* **103**, 093902 (2009).
- Peng, B. *et al.* Loss-induced suppression and revival of lasing. *Science* **346**, 328–332 (2014).
- Sun, Y., Tan, W., Li, H.-Q., Li, J. & Chen, H. Experimental demonstration of a coherent perfect absorber with PT phase transition. *Phys. Rev. Lett.* **112**, 143903 (2014).
- Dembowski, C. *et al.* Observation of a chiral state in a microwave cavity. *Phys. Rev. Lett.* **90**, 034101 (2003).
- Cao, H. & Wiersig, J. Dielectric microcavities: model systems for wave chaos and non-Hermitian physics. *Rev. Mod. Phys.* **87**, 61–111 (2015).
- Dembowski, C. *et al.* Experimental observation of the topological structure of exceptional points. *Phys. Rev. Lett.* **86**, 787–790 (2001).
- Lee, S.-B. *et al.* Observation of an exceptional point in a chaotic optical microcavity. *Phys. Rev. Lett.* **103**, 134101 (2009).
- Choi, Y. *et al.* Quasi-eigenstate coalescence in an atomic-cavity quantum composite. *Phys. Rev. Lett.* **104**, 153601 (2010).
- Heiss, W. D. Phases of wave functions and level repulsion. *Eur. Phys. J. D* **7**, 1–4 (1999).
- Dembowski, C. *et al.* Encircling an exceptional point. *Phys. Rev. E* **69**, 056216 (2004).
- Akis, R., Ferry, D. K. & Bird, J. P. Wave function scarring effects in open stadium shaped quantum dots. *Phys. Rev. Lett.* **79**, 123–126 (1997).
- Milner, V., Hanssen, J. L., Campbell, W. C. & Raizen, M. G. Optical billiards for atoms. *Phys. Rev. Lett.* **86**, 1514–1517 (2001).
- Kaplan, A., Friedman, N., Anderson, M. & Davidson, N. Observation of islands of stability in soft wall atom-optics billiards. *Phys. Rev. Lett.* **87**, 274101 (2001).
- Ponomarenko, L. A. *et al.* Chaotic Dirac billiard in graphene quantum dots. *Science* **320**, 356–358 (2008).
- Uzdin, R., Mailybaev, A. & Moiseyev, N. On the observability and asymmetry of adiabatic state flips generated by exceptional points. *J. Phys. A* **44**, 435302 (2011).
- Berry, M. V. & Uzdin, R. Slow non-Hermitian cycling: exact solutions and the Stokes phenomenon. *J. Phys. A* **44**, 435303 (2011).

Acknowledgements We thank M. Berry and O. Kirillov for comments. This research was supported by the Australian Research Council, the ImPACT Program of the Council for Science, Technology and Innovation (Cabinet Office, Government of Japan), the RIKEN iTHES Project, the MURI Center for Dynamic Magneto-Optics, a Grant-in-Aid for Scientific Research (type A), and the State of Bavaria.

Author Contributions E.A.O., T.G., E.E. and K.Y.B. conceived the idea for this research; T.G., E.E., M.D.F., R.G.D. and A.G.T. designed and built the experiment with conceptual contributions from E.A.O.; T.G., E.E. and R.G.D. collected and analysed experimental data; K.Y.B., E.E., T.C.H.L. and E.A.O. performed theoretical and numerical analysis; S.B., M.K., C.S. and S.H. fabricated and characterized the semiconductor microcavity; E.A.O. and K.Y.B. wrote the paper with input from T.G., E.E. and T.C.H.L.; F.N., M.D.F., A.G.T., S.H., Y.Y. and Y.S.K. contributed to discussions and the shaping of the manuscript.

Author Information Reprints and permissions information is available at www.nature.com/reprints. The authors declare no competing financial interests. Readers are welcome to comment on the online version of the paper. Correspondence and requests for materials should be addressed to E.A.O. (elena.ostrovskaya@anu.edu.au).

METHODS

Experimental setup. The semiconductor sample used in the experiment is a GaAs/AlGaAs microcavity containing 12 quantum wells (QWs) (~ 13 nm wide each) sandwiched between distributed Bragg reflector mirrors (32/36 mirror pairs). To achieve the strong interaction regime between cavity photons and quantum-well excitons^{1,31}, the quantum wells are distributed in the sample via three sets of four located at the anti-nodes of the photon mode. The cavity photon mode is red-detuned by 2.8 meV from the exciton resonance at 1.546 eV, resulting in the exciton-polariton dispersion schematically shown in Fig. 1a. The sample is mounted on a cold finger inside a continuous flow microscopy cryostat and maintained at 5.6 K.

A schematic of the experimental apparatus is shown in Extended Data Fig. 1. The exciton-polariton condensate is formed by illuminating the sample by a quasi-continuous, off-resonant, linearly polarized pump beam derived from a continuous wave (CW) Ti:sapphire laser operating at 732 nm. The threshold power for the condensation is ~ 0.079 mW μm^{-2} . To minimize heating of the sample, the pump beam is chopped by an acoustic optical modulator (AOM). We use a digital micromirror device (DMD) to engineer the spatial pump profile in the shape of a Sinai billiard shown in Fig. 1b, which is then re-imaged onto the sample at normal incidence through a high numerical aperture (NA) microscope objective.

Owing to the continuous decay of the exciton-polaritons, coherent photons escape the cavity as a photoluminescence signal and carry all the information about the condensate¹. The photoluminescence is then collected via the microscope objective and analysed using the CCD camera and spectrometer (Extended Data Fig. 1). We reconstruct the spatial modes by scanning the real space imaging across the slit of the spectrometer.

Creating exciton-polariton billiards. The DMD mirror is programmed to reflect the spatial pattern shown in Extended Data Fig. 2, thus creating a structured pump beam in the shape of a Sinai billiard³². The pump creates an inhomogeneous distribution of reservoir excitons in the plane of the quantum well, therefore inducing an effective potential for the condensed exciton-polaritons¹⁰.

The two parameters of the billiard controlling the non-Hermitian dynamics of exciton-polaritons are the radius of the round corner (defect), R , and the thickness of the walls, d . The latter is different on the different sides of the perimeter due to the shape of the laser beam illuminating the DMD. Throughout the main text, we consider a continuous change of R ($0 < R/W < 1$), but only two modifications of d (shown in Extended Data Fig. 2).

We have verified that, for any R , when the thickness of the walls is varied within our experimental range, the pump power density remains approximately constant. For the ‘thin’ and ‘thick’ wall configurations shown in Extended Data Fig. 2, the values are 0.110 ± 0.0033 mW μm^{-2} (Extended Data Fig. 2a) and 0.117 ± 0.0047 mW μm^{-2} (Extended Data Fig. 2b), respectively. This effectively means that the height of the billiard potential walls, defined by the pump power, remains the same. Since the internal area and hence geometry of the billiard does not depend on d either, this leads us to conclude that the wall thickness controls mainly the imaginary part of the billiard potential.

Spectroscopy of the billiard. Above the condensation threshold, exciton-polaritons occupy multiple energy levels of the billiard potential, and in our experiments we comfortably resolve approximately the first 15 levels in the energy versus position spectrum. As the radius of the defect in the Sinai billiard grows, the area of the potential confining exciton-polaritons shrinks, so that the energy levels are blueshifted (see Fig. 1c, d). The spectral line profiles measured at fixed spatial positions in the vicinity of degeneracy highlighted in Fig. 1c, d are shown in Extended Data Fig. 3. The line profiles obtained for several values of the defect radius within the range ($0.4 < R/W < 0.65$) are plotted on the same plot and their relative blueshift is represented by the offset on the intensity axis.

Positions of the individual energy levels (Fig. 2a, b) for different values of R are derived from the spectroscopic peaks, as schematically shown in Extended Data Fig. 3, and the linewidths (Fig. 2c, d) are determined by the numerical fitting of the spectral profile. The errors indicated in Fig. 2 arise from the numerical fitting procedure and therefore are very small.

Modelling of the billiard. The full dynamics of the exciton-polariton condensate subject to off-resonant, incoherent optical pumping can be described by the generalized complex Gross–Pitaevskii (or Ginzburg–Landau) equation^{33–35} for the condensate wavefunction, ψ :

$$i\hbar \frac{\partial \psi(\mathbf{r}, t)}{\partial t} = \left[-\frac{\hbar^2}{2m} \nabla^2 + (g - i\gamma_{nl})|\psi|^2 + (g_R + i\hbar R)n_R(\mathbf{r}) - i\hbar\gamma \right] \psi + i\hbar \Re[\psi(\mathbf{r}, t)] \quad (2)$$

Here m is the effective mass of the lower polariton, g is the polariton–polariton interaction strength, g_R is the strength of interaction between the reservoir and condensed polaritons, R is the rate of stimulated scattering into the condensed state, and γ is the spatially homogeneous decay rate of polaritons. The reservoir

density distribution $n_R(\mathbf{r}) \propto P(\mathbf{r})$ is defined by the rate of reservoir (excitonic) polariton injection per unit area and time, $P(\mathbf{r})$. The parameter γ_{nl} entering equation (2) characterizes gain saturation and, in general, depends on the spatial distribution of the pump. In our numerical calculations, we take the γ_{nl} to be small and spatially homogeneous due to the weak overlap between the condensate and the pumping area.

The model, equation (2), was initially suggested phenomenologically³³ and subsequently derived from the semiclassical Maxwell–Bloch equations³⁴. It qualitatively coincides with the generalized open-dissipative Gross–Pitaevskii model³⁶ augmented with the rate equation for the excitonic reservoir density:

$$\frac{\partial N_R}{\partial t} = P(\mathbf{r}) - (\gamma_R + R|\psi|^2)N_R$$

in the regime of near-threshold pumping³⁷. In this limit, the steady state reservoir density distribution can be expressed as $N_R \approx P(\mathbf{r})/\gamma_R - RP(\mathbf{r})|\psi|^2/\gamma_R^2 = n_R(\mathbf{r}) - \gamma_{nl}\hbar^{-1}R^{-1}|\psi|^2$, where γ_R is the decay rate of reservoir polaritons.

The phenomenological energy relaxation^{35,38,39}, which is essential to adequately model the multi-mode nature of the condensate³⁸, is taken in the following form^{35,38}:

$$\Re[\psi(\mathbf{r}, t)] = \alpha n_R \left[\mu(\mathbf{r}, t) - i\hbar \frac{\partial}{\partial t} \right] \psi(\mathbf{r}, t)$$

where α is the energy relaxation rate, and $\mu(\mathbf{r}, t)$ is a local chemical potential of the condensate.

We use equation (2) to obtain the structure of the spatial modes of the exciton-polariton condensate corresponding to peaks of the energy spectrum. The parameters of the model used for our dynamical simulations are as follows: $m = 5 \times 10^{-5} m_e$, where m_e is the free electron mass, $g = 2 \times 10^{-3}$ meV μm^2 , $g_R = 2g$, $\hbar R = 6 \times 10^{-4}$ meV μm^2 , $\gamma = 0.1$ ps⁻¹, $\gamma_{nl} = 0.3g$, $\alpha = 1.2 \times 10^{-3}$ μm^2 ps⁻¹ meV⁻¹. The effective potential height is $\max(V) = 2.25$ meV, and the billiard wall profile given by the reservoir density distribution, $n_R(\mathbf{r})$, is convoluted with a Gaussian profile to account for the ‘soft’ edges of the potential created by the optical excitation and exciton diffusion.

The spatial modes computed numerically using the fully nonlinear, open-dissipative dynamical model, equation (2), are presented in the bottom row of Extended Data Fig. 4. For comparison, the middle row of Extended Data Fig. 4 shows the single-particle eigenstates of the complex linear potential induced by the excitonic reservoir: $V(\mathbf{r}) = V' + iV'' \equiv g_R n_R(\mathbf{r}) + i\hbar[Rn_R(\mathbf{r}) - \gamma]$, with both real and imaginary parts V' , V'' proportional to the pumping rate³⁶, $P(\mathbf{r})$. One can see that the condensate dynamics described by equation (2) effectively populates the eigenstates of the linear complex effective potential. The validity of our model is confirmed by the excellent agreement with the experimental images of the billiard modes presented in the top row of Extended Data Fig. 4.

In agreement with previous studies⁴⁰, the nonlinearity due to exciton-polariton interactions strongly determines the relative population of the eigenstates, as well as the overall blueshift of the eigenenergies. The eigenenergies are complex, and so the spectral linewidths may exceed the level separation. For this reason, in our experiment some of the higher-order energy-filtered wavefunctions represent superpositions of neighbouring eigenstates. For example, the seventh mode measured in the experiment (last column in Extended Data Fig. 4) is, in fact, a superposition of eigenstates eight and nine, as revealed by the comparison with the numerically calculated modes. In contrast, the lower-order modes in Extended Data Fig. 4 represent almost pure eigenstates, having a very weak (less than 10%) admixture of the neighbouring eigenstates.

Hybridization of modes. Hybridization of modes occurs in the vicinity of crossing and anti-crossing of the energy levels in Fig. 2a and b. In these regions, the billiard modes are different in shape to the uncoupled modes away from the (near-)degeneracy. In experiments, it is hard to spectrally resolve pure modes in the hybridization region since their spectral linewidths exceed the peak separation. Therefore, what is experimentally imaged and shown in the insets of Fig. 2a and b is a superposition of two modes. This is especially true for Fig. 2b, where the spectral peaks (but not the linewidths) precisely coincide at the crossing, so that in the experiment we can only image a single mode corresponding to a single peak.

To match the spatial distributions obtained in the experiment with those found numerically, we plot superpositions of the pure eigenstates found in numerical simulations: $\varphi_s = \alpha\varphi_3 + \beta\varphi_4 e^{i\vartheta}$, where $\varphi_{3,4}$ are the pure eigenstates 3 and 4, α and β are their relative amplitudes, and ϑ is the relative phase. We find that only the relative phase $\vartheta = \pi/2$ can produce a superposition that fits well with the experiment. These spatial modes (pure and superposition states) for the thick and thin billiard in the hybridization region (anti-crossing and crossing of eigenenergies, respectively) are shown in Extended Data Fig. 5.

Note that this mode mixing is performed only in the hybridization region. Away from this region, the experimentally imaged and numerically calculated modes

match extremely well. Importantly, in Fig. 4, in order to perform a reliable phase extraction from numerically found modes away from the (near-)degeneracy, it is absolutely necessary to trace the continuous variation of phase of the pure modes as we pass the hybridization region. For this reason, we did not mix numerically found pure modes to match experimentally imaged spatial distributions of superposition states. This explains visible discrepancies between the spatial structure of numerically calculated and experimentally imaged modes in the hybridization regions in Fig. 4.

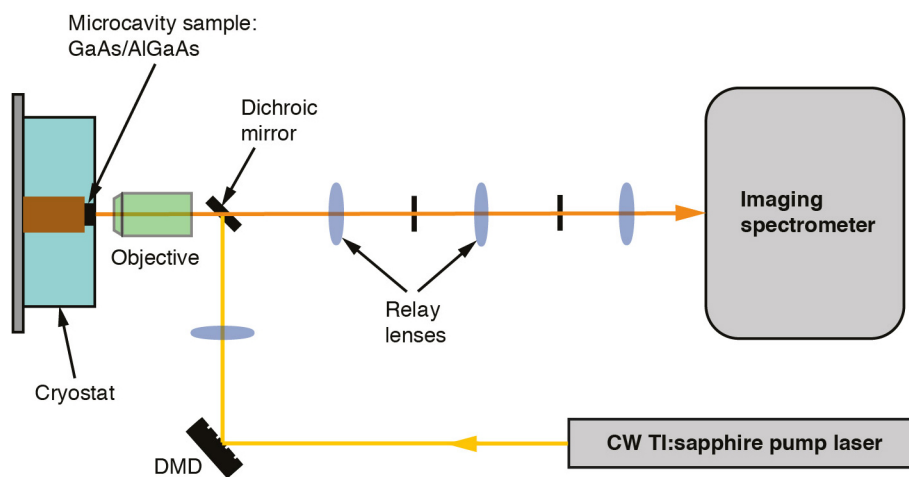
Coupled-mode model. The behaviour of any two non-Hermitian modes of the billiard potential near the degeneracy point can be described by a standard coupled-mode model written in the dimensionless form as follows:

$$i \frac{\partial \psi_{n,n'}(\mathbf{r}, t)}{\partial t} = [-\nabla^2 + V'(\mathbf{r}) + iV''(\mathbf{r})] \psi_{n,n'} + \Omega \psi_{n',n} \quad (3)$$

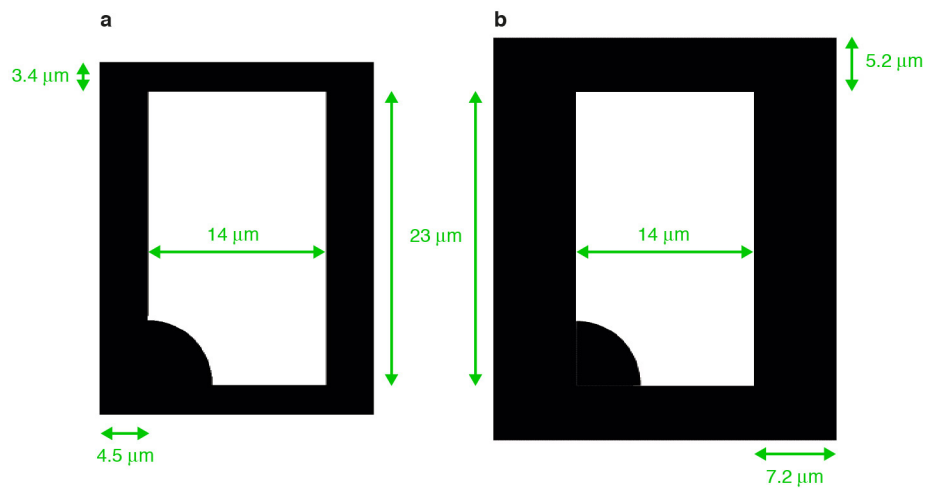
where Ω characterizes the coupling strength between the states n and n' . Separating the temporal and spatial dependence of the wavefunctions, $\psi_n = a_n(t)\varphi_n(\mathbf{r})$, substituting this ansatz into equation (3), and integrating out the spatial degrees of freedom, leads us to the eigenvalue equation (1) in the main text, where $(n, n') = (1, 2)$. The real energies of the modes away from the degeneracy in equation (1) are defined by the shape of the billiard potential, $[-\nabla^2 + V'(\mathbf{r})]\varphi_n(\mathbf{r}) = E_n\varphi_n(\mathbf{r})$, the complex parts of the eigenenergies are given by the overlap between the billiard modes and the exciton reservoir, $\Gamma_n \propto \int V''(\mathbf{r})|\varphi_n(\mathbf{r})|^2 d^2r$, and the off-diagonal matrix elements in equation (1) are determined by the degree of spatial overlap between the two modes, $q \propto \int \varphi_n^*(\mathbf{r})\varphi_{n'}(\mathbf{r}) d^2r$. Here we assume that the uncoupled modes are properly normalized.

We stress that our theory essentially uncovers the non-Hermitian features of degeneracies of the modes of the entire billiard, which can be considered as a two-dimensional resonator in the plane of the quantum well. This approach is conceptually close to, for example, the theory of two-dimensional PT-symmetric systems⁴¹ and differs from the well developed coupled-mode theories for weakly coupled non-Hermitian single-mode resonators.

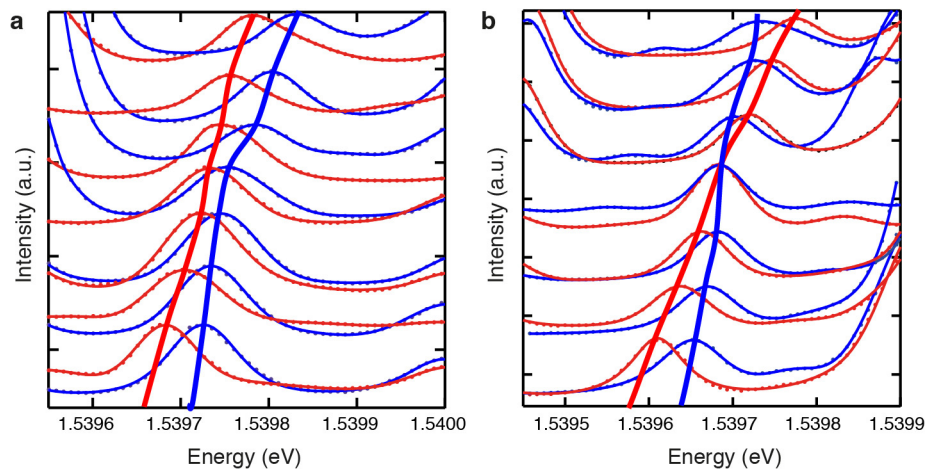
31. Kavokin, A., Baumberg, J., Malpuech, G. & Laussy, F. *Microcavities* (Oxford Univ. Press, 2007).
32. Sinai, Y. G. Dynamical systems with elastic reflections. *Russ. Math. Surv.* **25**, 137–189 (1970).
33. Keeling, J. & Berloff, N. G. Spontaneous rotating vortex lattices in a pumped decaying condensate. *Phys. Rev. Lett.* **100**, 250401 (2008).
34. Cristofolini, P. *et al.* Optical superfluid phase transitions and trapping of polariton condensates. *Phys. Rev. Lett.* **110**, 186403 (2013).
35. Askitopoulos, A. *et al.* A robust platform for engineering pure-quantum-state transitions in polariton condensates. *Phys. Rev. B* **92**, 035305 (2015).
36. Wouters, M. & Carusotto, I. Excitations in a nonequilibrium Bose–Einstein condensate of exciton polaritons. *Phys. Rev. Lett.* **99**, 140402 (2007).
37. Smirnov, L. A., Smirnova, D. A., Ostrovskaya, E. A. & Kivshar, Yu. S. Dynamics and stability of dark solitons in exciton-polariton condensates. *Phys. Rev. B* **89**, 235310 (2014).
38. Wouters, M. Energy relaxation in the mean-field description of polariton condensates. *New J. Phys.* **14**, 075020 (2012).
39. Wertz, E. *et al.* Propagation and amplification dynamics of 1D polariton condensates. *Phys. Rev. Lett.* **109**, 216404 (2012).
40. Eastham, P. R. Mode locking and mode competition in a nonequilibrium solid-state condensate. *Phys. Rev. B* **78**, 035319 (2008).
41. Ge, L. & Stone, A. D. Parity-time symmetry breaking beyond one dimension: the role of degeneracy. *Phys. Rev. X* **4**, 031011 (2014).



Extended Data Figure 1 | Diagram of the experimental apparatus. See Methods for details.

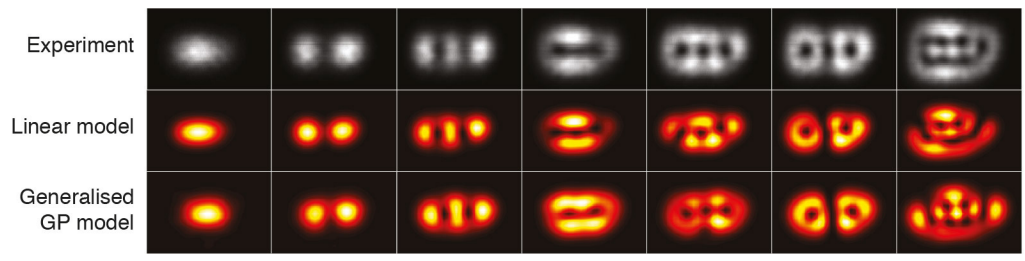


Extended Data Figure 2 | Schematics of the optically induced billiard potential with two different wall thicknesses. **a**, Thin walls; **b**, thick walls. The active regions corresponding to the optical pump are shown in black, and we note that the enclosed area does not change with wall thickness.



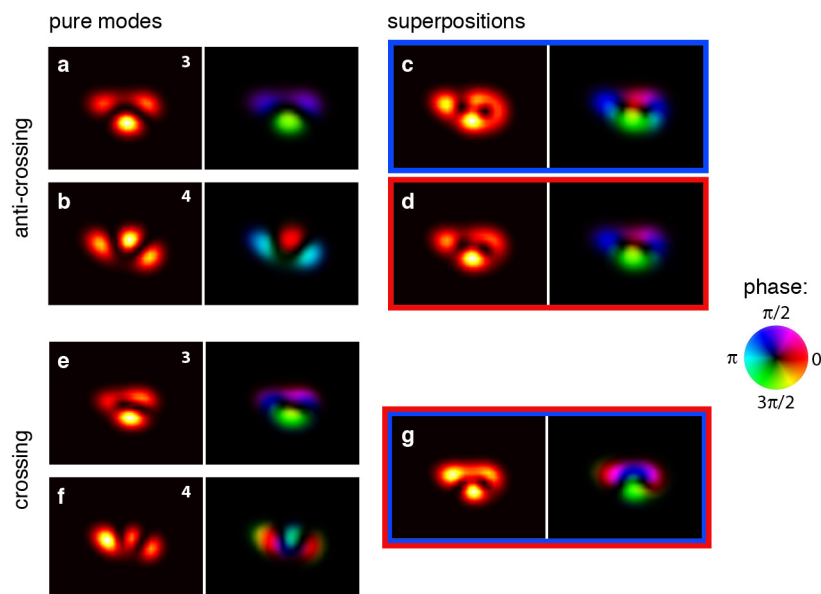
Extended Data Figure 3 | Effect of wall thickness on spectroscopic line profiles of the Sinai billiard. **a, b,** Profiles are shown in the vicinity of the degeneracy for the levels highlighted in Fig. 1c, d with thick (**a**) and thin

(**b**) walls. The thick lines demonstrate the principle of data extraction for anti-crossing (**a**) and crossing (**b**) of the energy levels corresponding to those shown in Fig. 2a and b, respectively



Extended Data Figure 4 | Spatial density distribution of the first seven simultaneously populated lowest-energy modes of the Sinai billiard. Spatial density distributions were obtained from the thick-wall setup (Extended Data

Fig. 2b) with $R/W = 0.35$. Top row, experimentally imaged; middle row, calculated using the effective linear potential model; bottom row, calculated using the full dynamical model given by equation (2).



Extended Data Figure 5 | Spatial modes in the hybridization regions. **a–g**, Calculated spatial modes; each panel shows the modulus squared of the wavefunction (left) and the wavefunction's phase distribution (right, colour coded). **a**, **b**, **e**, **f**, Numerically calculated pure spatial eigenstates (modes 3 (**a**, **e**) and 4 (**b**, **f**)) for the Sinai billiard with thick and thin walls in the corresponding hybridization regions shown in Fig. 2a and b, respectively.

c, **d**, **g**, The superpositions of modes 3 and 4 that match the experimentally imaged modes shown in Fig. 2; **c** (boxed in blue) and **d** (boxed in red) correspond to the blue and red curves of Fig. 2a, respectively, while **g** (boxed in red and blue) corresponds to the crossing point in Fig. 2b. The relative populations of pure modes in the superposition states are: **c**, $|\alpha|^2 = 0.85$ and $|\beta|^2 = 0.15$; **d**, $|\alpha|^2 = 0.65$ and $|\beta|^2 = 0.35$; **g**, $|\alpha|^2 = 0.60$ and $|\beta|^2 = 0.40$.